bioRxiv preprint doi: https://doi.org/10.1101/2020.08.30.273748; this version posted August 31, 2020. The copyright holder for this preprint (which was not certified by peer review) is the author/funder. All rights reserved. No reuse allowed without permission.

Sequence-encoded and Composition-dependent Protein-RNA Interactions Control Multiphasic Condensate Topologies

Taranpreet Kaur[a], Muralikrishna Raju[b§], Ibraheem Alshareedah[a§], Richoo B. Davis[a], Davit A. Potoyan*[b], Priya R. Banerjee*[a]

[a]Department of Physics, University at Buffalo, Buffalo NY 14260, USA
[b]Department of Chemistry, Iowa State University, Ames IA 50011, USA
§These authors contributed equally

*Corresponding Authors:

Priya R. Banerjee: prbanerj@buffalo.edu
Davit A. Potoyan: potoyan@iastate.edu

bioRxiv preprint doi: https://doi.org/10.1101/2020.08.30.273748; this version posted August 31, 2020. The copyright holder for this preprint (which was not certified by peer review) is the author/funder. All rights reserved. No reuse allowed without permission.

ABSTRACT

Multivalent protein-protein and protein-RNA interactions are the drivers of biological phase separation. Bio-condensates typically contain a dense network of multiple proteins and RNAs, yet the role of overlapping molecular interactions in regulating the condensate composition and structure is not well understood. Employing a ternary system comprising of a prion-like polypeptide (PLD), arginine-rich polypeptide (RLD), and RNA, here we show that competition between the PLD and RNA for a single shared partner, the RLD, leads to PLD–RLD demixing and spontaneous formation of biphasic condensates. Combining experiments with simulations, we show that the topology of coexisting condensates is regulated via mixture composition and the nature of protein-protein and protein-RNA interactions, giving rise to a diverse set of multiphasic patterns including completely separated, partially and completely engulfed droplet morphologies, and Janus droplets. Our findings provide a minimal set of physical rules that govern the composition and spatial organization of multicomponent and multiphasic bio-condensates.

bioRxiv preprint doi: https://doi.org/10.1101/2020.08.30.273748; this version posted August 31, 2020. The copyright holder for this preprint (which was not certified by peer review) is the author/funder. All rights reserved. No reuse allowed without permission.

In biological cells, many multivalent ribonucleoproteins (RNPs) form biomolecular condensates (BMCs) that act as active or repressive hubs for intracellular storage and signaling[1,2]. These condensates can rapidly assemble and dissolve in response to cellular stimuli via a physical process known as liquid-liquid phase transition[3-5]. The functional specificity of BMCs as subcellular organelles is linked to selective enrichment of specific enzymes/signaling factors within[1,6], whereas altered compositions of signaling condensates are associated with disease pathologies[2,4,7-9]. Mounting evidence now suggest that the spatial organization of biomolecules into distinct sub-compartments within BMCs [*e.g.*, nuclei[10,11], nuclear speckles[12], paraspeckles[13] and stress granules[14]] adds another layer of internal regulation of composition and plays a fundamental role in facilitating their complex biological functions. These mesoscopic multilayered structures can be qualitatively understood on the basis of a multi-phasic condensate model, where two or more distinct types of partially immiscible condensed phases are formed by spontaneous phase separation of individual components in a multi-component mixture[11,15,16]. However, due to the complexities generated by the presence of a large number of distinct protein and RNA components in a typical intracellular BMC, the underlying molecular mechanisms that regulate the multiphasic condensate composition and spatial organization remain largely unexplored.

The composition and spatial organization of BMCs are ultimately controlled by the nature of intermolecular interactions between RNPs and RNAs as well as their interactions with the solvent molecules[2,11,17,18]. Analysis of sequence features of eukaryotic BMC proteins revealed that intrinsically disordered low complexity domains (LCDs) are common drivers and/or regulators of RNP phase separation with and without RNAs[19-23]. The LCD sequence composition and patterning provide programmable modules for dynamic multivalent protein-protein and protein-RNA interactions[24-29]. In multi-component mixtures, these dynamic inter-chain interactions are ubiquitous and can either cooperate or compete within a dense network of LC proteins and RNAs[30,31]. The presence of multiple RNPs and RNAs within an intracellular BMC highlights the relevance of understanding how networks of overlapping interactions control the condensate composition and structure[32], given these very properties are intricately linked to their functional output in the cell[2].

To systematically explore the regulatory principles of multicomponent RNP condensation with overlapping protein-protein and protein-RNA interactions, here we employ a minimalistic three-component system composed of two LC disordered polypeptides: a prion-like LCD (PLD) and an Arg-rich LCD (RLD), and RNA. PLDs are typically characterized by the presence of π electron-rich amino acids (Y/P/Q/G/S; examples: hnRNPA1, TDP43, FUS)[23], whereas R-rich LCDs are promiscuous RNA binders and commonly occur as intrinsically disordered RGG domains[22,33] (examples: G3BP1, LSM14A, hnRNPDL, EWSR1, FUS, TAF15). Both LCD types are highly abundant in stress granule and processing body proteins[34] — the two major cytoplasmic BMCs in eukaryotes. From a pathological point of view, multivalent R-rich repeat polypeptides, such as poly(GR) and poly(PR), are potent neurotoxins and are directly linked to c9orf72-derived repeat expansion disorder[35-41]. These R-rich repeat polymers can invade SGs and impair their fluid dynamics by aberrantly interacting with SG

bioRxiv preprint doi: https://doi.org/10.1101/2020.08.30.273748; this version posted August 31, 2020. The copyright holder for this preprint (which was not certified by peer review) is the author/funder. All rights reserved. No reuse allowed without permission.

components, including PLDs and RNAs[29,42-44]. Within the PLD-RLD-RNA system, three interactions have the capacity to drive independent phase separation processes: PLD-PLD interactions can drive homotypic PLD phase separation[23,45], PLD-RLD interactions can drive the co-phase separation of PLD-RLD into heterotypic condensates[46], and RLD-RNA interactions can drive the formation of RLD-RNA condensates[28,47,48]. Therefore, the RLDs within the PLD-RLD-RNA system represent promiscuous modules that can interact with both PLDs and RNAs[42,43,46]. As such, the PLD-RLD-RNA ternary system represents a suitable and biologically relevant triad for dissecting how networks of overlapping biomolecular interactions control the condensate composition and structure.

Here, employing a multi-scale approach, we systematically study the role of competitive protein-protein and protein-RNA interactions in controlling the topology of ternary PLD-RLD-RNA condensates. For two-component systems (PLD-RLD and RLD-RNA), we show that the mixture composition is a key factor in controlling the phase behavior, condensate spatial organization, and client recruitment in a context-dependent manner. Specifically, we show that for PLD-RLD mixtures, RLD *monotonically* enhances PLD condensation. On the contrary, RLD-RNA mixtures display a reentrant phase behavior in which the RNA-to-RLD mixing ratio determines the surface organization of RLD-RNA binary condensates in a *highly non-monotonic fashion*. Within the PLD-RLD-RNA ternary system, RNA-RLD interactions dominate over PLD-RLD interactions, leading to an RNA-induced demixing of PLD-RLD condensates into stable coexisting phases (homotypic PLD condensates and heterotypic RLD-RNA condensates). The topology of these biphasic condensates (non-engulfing/ partial engulfing/ complete engulfing) is determined by the RNA-to-RLD stoichiometry and the hierarchy of intermolecular interactions, providing a glimpse of the broad range of multiphasic patterns that are accessible to these condensates. Mechanistically, the multiphasic structuring of PLD-RLD-RNA condensates is governed by the molecular interactions at the liquid-liquid interfaces, which are encoded in the amino-acid sequence of the proteins and regulated by the composition of the mixture. This multi-scale regulation of inter-condensate surface interactions controls the relative interfacial tensions between the three liquid phases (PLD condensed phase, RLD-RNA condensed phase, and the dispersed phase). Together, our findings reveal that overlapping intermolecular interactions in a multicomponent system represent a regulatory paradigm for controling the composition and structure of multiphasic bio-condensates.

RESULTS AND DISCUSSION

Mixture composition controls the structure and dynamics of binary condensates

Before probing the ternary PLD-RLD-RNA phase separation, we studied the phase behavior of the three corresponding binary mixtures: PLD-RLD; PLD-RNA; and RLD-RNA. The presence of R-rich RNA binding domains has been reported to enhance PLD phase separation through intermolecular Arg-Tyr interactions[42,46]. To quantify such an effect in our PLD-RLD binary system, we first determined the isothermal state diagram of the FUS^{PLD} in the presence of arginine/glycine-rich polypeptides (RLD: $[RGRGG]_5$ and

bioRxiv preprint doi: https://doi.org/10.1101/2020.08.30.273748; this version posted August 31, 2020. The copyright holder for this preprint (which was not certified by peer review) is the author/funder. All rights reserved. No reuse allowed without permission.

FUS^{RGG3}; **Table S2**). Our analysis revealed that PLD undergoes heterotypic phase separation with RLD in a composition-dependent manner. Specifically, the LLPS concentration threshold for PLD (C_{LLPS}^{PLD}) decreases monotonically with increasing RLD concentration [in the absence of the RLD, C_{LLPS}^{PLD} = $C_{saturation}^{PLD}$ ~ 240 μM; at RLD-to-PLD ratio of 5, C_{LLPS}^{PLD} ~ 120 μM] (**Fig. 1a; Fig. S1**). Furthermore, confocal microscopy imaging and fluorescence recovery after photobleaching (FRAP) assays indicate that the PLD partition coefficient and mobility within PLD-RLD condensates scale monotonically with increasing RLD concentration (**Fig. 1b&c**, **Figs. S2&S3**). Taken together, our experiments show that with increasing RLD concentration, PLD apparent diffusion coefficient (D_{app}) along with the LLPS threshold concentration (C_{LLPS}^{PLD}) decrease while PLD partition coefficient (K) increases (**Fig. 1a-c** and **Fig. S3**). These results are consistent with previous literature reports[42,46] and indicate that RLDs significantly enhance PLD phase separation and impact the condensate dynamics (**Fig. 1a-c**). However, in contrast to PLD-RLD mixtures, the isothermal state diagram of PLD-RNA mixtures [utilizing a homopolymeric RNA, poly(U)] showed that RNA does not have any significant impact on PLD phase separation (**Fig. S4a).** We independently confirmed that poly(U) RNA does not significantly interact with the PLD by using fluorescence correlation spectroscopy (FCS), which revealed identical PLD autocorrelation curves in the absence and presence of poly(U) RNA (**Fig. S4b**).

Similar to RLD-PLD mixtures, RLD-RNA mixtures display a composition-dependent phase behavior. However, unlike RLD-PLD mixtures, their phase behavior is highly non-monotonic, wherein the two-phase regime is only stabilized within a small window of mixture compositions (**Fig. 1d**). Such phase behavior is usually referred to as reentrant phase transition[28,47,49]. Within the reentrant phase separation window (**Fig. 1d**), we previously predicted that disproportionate mixture compositions may lead to the formation of "micellar" condensates, in which the condensates' surfaces can be either enriched in RLDs or RNAs depending on the mixture stoichiometry[49]. To validate the micellar condensate formation in our system, we performed molecular dynamics (MD) simulations using a single-residue resolution coarse-grained model of an RLD from an archetypal ribonucleoprotein FUS (FUS^{RGG3}) and a homopolymeric RNA, poly(U)[49] (**Table S2**). The representative equilibrium structures of the RLD-RNA condensates revealed two distinct condensate architectures: (a) condensates with RLD-enriched surfaces at $C_{RNA} < C_{RLD}$, and (b) condensates with RNA-enriched surfaces at $C_{RNA} > C_{RLD}$ (**Fig. 1d, Fig. S5**). Therefore, these condensates appear to be spatially organized[49] and their surface composition is dynamically varied in an RNA dose-dependent manner.

Since RLD chains, but not RNA chains, multivalently interact with the PLD chains (**Figs. 1a-c and S4**), we next considered the potential of RLD-RNA condensates to deferentially recruit prion-like clients based on their surface architecture. We hypothesize that RLD-rich condensates, but not the RNA-rich condensates, would positively recruit PLDs. Furthermore, the recruited PLDs are expected to be localized on the surface of RLD-rich condensates due to the availability of free RLD sites (**Fig. 1e**). Performing MD simulations similar to those in **Figure 1d** but now including π-rich FUS^{PLD} as a client (**Table S2**), we observed enhanced surface recruitment of PLD chains into RLD-RNA droplets at low-RNA conditions, while high-RNA conditions resulted in no recruitment of

bioRxiv preprint doi: https://doi.org/10.1101/2020.08.30.273748; this version posted August 31, 2020. The copyright holder for this preprint (which was not certified by peer review) is the author/funder. All rights reserved. No reuse allowed without permission.

PLD clients into RLD-RNA condensates (**Fig. 1f, Fig. S6)**. Experimentally, we utilized PLDs from two different RNPs, EWS and FUS, and quantified their partitioning in FUS^{RGG3}-poly(U) condensates (**Table S2**). Briefly, we formed RNA-RLD condensates at variable RNA-to-RLD mixing ratios in a buffer that contains the desired PLD clients (labeled with Alexa488 dye). Confocal fluorescence microscopy assays showed that both PLDs are preferentially recruited into RLD-RNA condensates at $C_{RLD} > C_{RNA}$ while the same clients showed no preferential patitioning into the RLD-RNA condensates at $C_{RLD} < C_{RNA}$ (**Fig. 1g&h, Figs. S7&S8**). Analysis of these fluorescence micrographs reveals a ~10-fold increase in the partition coefficient of PLDs in RLD-rich condensates as compared to RNA-rich condensates (**Fig. 1g-h&k**). Furthermore, inspecting the fluorescence intensity profiles across RLD-rich condensates revealed that PLDs are preferentially recruited on the condensates' surface while being relatively depleted from the condensates' core (**Fig. 1j**). These observations confirm that the PLD recruitment in RLD-rich condensates is mediated by molecules on the surface which are predominantly, as our simulation suggests, unbound segments of RLDs (**Fig. 1d**). To test the generality of this phenomenon, we next performed similar analysis with two additional client polypeptides with similar sequence features as FUS and EWS PLDs: the P/S/G/Q-rich LCD of a transcription activator BRG1 (AA: 1-340) and the C-terminal LCD of RNA polymerase II (Pol II CTD) which contains 30 repeats of YSPTSPS (**Table S2**). Both $BRG1^{LCD}$ and Pol II CTD are enriched in amino acid residues which have exposed π-containing peptide backbones[21]. In addition, Pol II CTD is also enriched in Tyrosine residues (**Table S2**). Thus, both $BRG1^{LCD}$ and Pol II CTD are expected to interact with RLDs through Arg-π contacts and therefore display RNA-dependent recruitment into spatially organized RLD-RNA condensates. This prediction was verified experimentally using our confocal microscopy assay (**Fig 1i-k, Fig. S9&10**).

Collectively, our analysis of the phase separation behavior of different binaries in the PLD-RLD-RNA ternary system reveals two significant pairwise interactions: PLD-RLD and RLD-RNA. While the mixture composition in the PLD-RLD system monotonically impacts PLD-RLD condensate dynamics, in the RLD-RNA binary system, it controls the RLD-RNA condensate architecture. The stoichiometry-dependent recruitment of PLD clients and their spatial localization within RLD-RNA condensates highlights that RNA is capable of regulating PLD-RLD interactions by controlling the availability of free RLD chains on the surface of these condensates (**Fig. 1e**). To investigate this regulatory effect of RNA on PLD-RLD interactions further, we next examined the impact of RNA on the phase behavior of heterotypic PLD-RLD condensates.

RNA induces condensate switching from PLD-RLD to RLD-RNA droplets

To probe for the effect of RNA on the heterotypic PLD-RLD condensates, we first generated PLD-RLD condensates at a PLD concentration *lower than* the homotypic PLD LLPS concentration ($C_{PLD} < C_{sat}$; the green region in the state diagram in **Fig 1a**). Two-color fluorescence time-lapse imaging showed that the addition of poly(U) RNA to PLD-RLD phase separated mixture leads to the dissolution of PLD-RLD droplets and subsequent formation of RLD-RNA droplets (**Fig 2a&b, Movie S1**). The dissolution of PLD-RLD droplets is preceded by a change in their color from yellow (RLD+PLD) to green

bioRxiv preprint doi: https://doi.org/10.1101/2020.08.30.273748; this version posted August 31, 2020. The copyright holder for this preprint (which was not certified by peer review) is the author/funder. All rights reserved. No reuse allowed without permission.

(PLD), indicating that RLD is leaving these droplets and hence weakening the condensate network and leading to their dissolution (**Fig 2b**). This condensate switching behavior (from PLD-RLD to RLD-RNA condensates) in the presence of RNA signifies a competition between RLD-PLD and RLD-RNA interactions, with RLD-RNA interactions being stronger than RLD-PLD interactions (**Fig. 2a**). To investigate whether this effect is specific to poly(U) RNA, we repeated the same assay using poly(A) RNA. Confocal video microscopy revealed that poly(A) RNA is also able to induce the observed condensate switching by sequestering RLDs out of PLD condensates and subsequently forming RLD-RNA condensates (**Fig. 2c**). Collectively, these results suggest that RNA can induce a condensate-switching transition from PLD-RLD condensates to RLD-RNA condensates due to its superior interactions with the RLD.

RNA triggers a de-mixing transition of RLD and PLD

Our observations in **Figure 2** indicate that RNA can sequester RLD out of PLD condensates, which leads to the dissolution of PLD condensates. We therefore asked whether forming PLD-RLD condensates at PLD concentration (C_{PLD}) greater than PLD saturation concentration ($C_{PLD} > C_{sat}$; the pink region in the state diagram in **Fig 1a; Fig S1**), would alter the observed RNA-triggered condensate switching effect (**Fig. 2**). Repeating our measurements under such conditions, we observed a de-mixing transition, where PLD-RLD condensates reorganized into homotypic PLD condensates and heterotypic RLD-RNA condensates in response to RNA addition (**Fig 3a&b, Movie S2, Fig. S11**). The time-lapse images reveal that RNA sequesters RLD (red) from PLD-RLD droplets, reaffirming the apparent dominance of RLD-RNA interactions over RLD-PLD interactions. Following the sample equilibration upon RNA addition, we observed that PLD condensates and the newly formed RLD-RNA condensates coexist in a multiphasic pattern where RLD-RNA droplets are distributed on the surfaces of PLD droplets (**Fig 3c**). To confirm that the multiphasic condensate formation is not an artifact due to the order of RNA addition, we mixed pre-formed PLD condensates ($C_{PLD}>C_{saturation}$) with RLD-RNA condensates (prepared independently) and imaged them using a confocal microscope. We observed that PLD condensates coexist with RLD-RNA condensates in a multiphasic pattern that is reproducible irrespective of the method of sample preparation (**Fig. S12**) and is stable for more than 24 hours (**Fig. S13**). We also confirmed that our results are not specific to poly(U) RNA by repeating these experiments with a considerably shorter RNA chain U_{40} and poly(A) RNA (**Fig. 3e&f**).

The co-existing condensates (e.g., PLD and RLD-RNA), although quite dynamic as indicated by their respective coalescence-induced condensate growth (**Fig. S14**), do not exchange their components. Based on these observations, we hypothesized that these coexisting condensates can support distinct microenvironments and differentially recruit specific client biomolecules accordingly, and that the RNA-induced condensate demixing may represent a pathway for sorting those client biomolecules in different condensates (**Fig. 3g**). Indeed, we observed that a short fluorescently-labeled RNA client (5'-FAM-UGAAGGAC-3') and a protein client (Pol II CTD) that simultaneously partition into PLD-RLD droplets in absence of any RNA are differentially sorted into coexisting condensates in the presence of RNA. More specifically, we observed that the RNA client

bioRxiv preprint doi: https://doi.org/10.1101/2020.08.30.273748; this version posted August 31, 2020. The copyright holder for this preprint (which was not certified by peer review) is the author/funder. All rights reserved. No reuse allowed without permission.

partitions into the RLD-RNA droplet and the Pol II CTD is uptaken by the PLD droplets (**Fig. 3h**). Taken together, these results suggest that the competition between RLD-RNA and RLD-PLD intermolecular interactions in a ternary PLD-RLD-RNA mixture can give rise to a rich multiphasic behavior that constitutes condensate switching, condensate demixing, and client sorting (**Figs. 2&3**).

Mixture composition tunes the topology of coexisting PLD and RNA-RLD condensates

Multi-phasic structures, which stem from the coexistence of multiple immiscible liquid phases[50-52], are hallmarks of several subcellular biomolecular condensates such as the nucleolus and stress granules[11,14,53]. For a three-phase-system (such as A-droplets, B-droplets, and C-dispersed liquid phase), the equilibrium spatial configuration is determined by the relative interfacial tensions (γ_{AC}, γ_{BC}, and γ_{AB}) of the three liquid phases[11,15,16]. Based on the rank order of γ_{AC}, γ_{BC}, and γ_{AB}, three configurations are possible (**Fig. 4a**): (i) condensates do not share any interface and remain separated ($\gamma_{AB} > \gamma_{AC} + \gamma_{BC}$; non-engulfment); (ii) condensates partially merge in a way that they share a common interface but are still partly exposed to the dispersed liquid phase ($\gamma_{AC} \sim \gamma_{BC} \sim \gamma_{AB}$; partial engulfment); and (iii) condensate A resides within the condensate B and remains completely separated from the dispersed liquid phase ($\gamma_{AC} > \gamma_{BC} + \gamma_{AB}$ or vice-versa; complete engulfment).

Our experimental results in **Figure 1d-k** showed that the surface architecture of RLD-RNA condensates is tuned by RNA-to-RLD stoichiometry, resulting in a switch-like change of PLD interactions with these condensates. This raises an interesting possibility of regulating interfacial interactions between RLD-RNA condensates and PLD condensates, given that RLD, but not RNA, multivalently interacts with PLDs. As such, increasing RNA concentration may lead to a controlled morphological variation in the coexisting PLD and RLD-RNA condensates. To test this possibility, we reconstituted the condensate pair by mixing homotypic PLD condensates with preformed RNA-RLD condensates prepared at a variable RNA-to-RLD stoichiometry. We chose RNA-to-RLD ratios such that they span the entire range of the reentrant RNA-RLD LLPS regime (**Fig. S15**). We observed that the RLD-rich condensates ([RNA]:[RLD] = 0.1, 0.2, 0.75) are almost completely engulfed by the PLD homotypic droplets (**Fig 4b**). On the contrary, RNA-rich condensates ([RNA]:[RLD] = 1.25, 2.5, and 5.0) are only partially engulfed by PLD droplets with a shared interface between the two condensate types that substantially decreases with increasing RNA concentration (**Fig 4b**). To quantify the variation in the interfacial patterning of the two condensate types with changing RNA-to-RLD ratio, we estimated the contact angles for both PLD (θ_{PLD}) and RLD-RNA (θ_{RLD}) droplets using an image analysis approach (*see* Materials and Methods; **Fig. 4c**). The cosine of a contact angle (θ), defined as the dihedral angle formed by a liquid interface at the three-phase boundary, is a function of the interfacial tension of the three liquid phases[50,54].

$$\cos(\theta_{PLD}) = \frac{\gamma_{RLD}^2 - \gamma_{PLD}^2 - \gamma_{PLD-RLD}^2}{2\gamma_{PLD}\gamma_{PLD-RLD}} \quad (1)$$

A small θ_{PLD} indicates that PLD phase is engulfing RLD phase partially and the contact area between the two droplets is significant. On the other hand, a large value of θ_{PLD}

bioRxiv preprint doi: https://doi.org/10.1101/2020.08.30.273748; this version posted August 31, 2020. The copyright holder for this preprint (which was not certified by peer review) is the author/funder. All rights reserved. No reuse allowed without permission.

indicates that the two phases do not have a significant preference for a shared interface (**Fig. c,** *top panel*). Remarkably, we observed a sigmoidal-like transition of PLD contact angle (θ_{PLD}) as the RNA-to-RLD ratio is increased, while the RLD contact angle (θ_{RLD}) remained unchanged (**Fig. 4c,** *bottom panel*). Thus, variation in θ_{PLD} quantifies the transition in the coexistence pattern observed in **Figure 4b** with increasing RNA concentration. According to equation-1, the observed variation in the PLD contact angle indicates a change in the relative rank order of the interfacial tensions in the three-phase system[50]. To confirm this finding, we performed computer simulations utilizing a fluid-interface modeling tool [Surface Evolver [55]]. Briefly, we created equal volumes of two immiscible liquids with specified interfacial tensions and minimized the total energy of the system by modifying the shape of each liquid interface (*see* Materials and Methods; **Fig. S16a**). As the relative magnitude of the interfacial tension between the two condensates (i.e., $\gamma_{PLD-RLD}$) increased, we observed that the droplets transitioned from a completely engulfed morphology to a partially engulfed state and subsequently to a non-engulfing state (**Fig. 4d**), similar to our experimentally observed morphological transition with RNA concentration (**Fig. 4b**). By comparing the results in **Figure 4d** with those in **Figure 4b**, we conclude that increasing the RNA concentration energetically destabilizes the shared interface between PLD droplets and RLD-RNA droplets.

A molecular mechanism that explains the effect of RNA on regulating the coexistence pattern can be deduced from the consideration that the surface organization of RNA-RLD condensates is altered as a function of the RNA-to-RLD mixing ratio (**Fig. 1d-e**). At low RNA-to-RLD ratio, the surface enrichment of free and/or partially-condensed RLDs (**Fig. 1d**) confers a high propensity for the RLD-RNA condensates to favorably interact with the homotypic PLD condensates (**Fig. 4e**) through PLD-RLD interfacial binding (**Fig. 1d-f**). However, at high RNA-to-RLD concentration ratio, the surface of RLD-RNA condensates is enriched with free/partially-condensed RNA chains (**Fig. 1d**), rendering the interfacial interactions between PLD and RLD-RNA droplets significantly less favorable (**Fig. 4e**; **Fig. S4**). Consequently, the interfacial tension between the two types of condensates (PLD and RLD-RNA) is expected to increase. Therefore, as the RNA-to-RLD ratio increases, a progressive decrease in the contact area between the two condensates takes place (**Fig. 4b-e**). To test this idea, we used molecular dynamics simulations utlizing homotypic PLD condensates and RLD (FUS^{RGG3})-RNA condensates. The simulated equilibrium structures (**Fig 4f, Fig. S16b**) show that with increasing RNA concentration, a progressive morphological transition occurs wherein the coexistence pattern of PLD and RLD-RNA droplets transitions from complete engulfment to partial engulfment to completely separated (non-engulfment) topologies. Taken together with the MD simulations shown in **Figure 1d&f**, these results further validate that relative RNA concentration (*i.e.*, RNA-to-RLD stoichiometry) plays a central role in determining topologies of multiphasic condensates (**Figs. 4b-d&f**).

Sequence-encoded protein-protein and protein-RNA interactions determine multiphasic condensate structuring

Our results in **Figure 1** and **Figure 4** indicate that PLD-RLD interactions (or a lack thereof) at the liquid-liquid interface determines the stability of the interface between PLD

bioRxiv preprint doi: https://doi.org/10.1101/2020.08.30.273748; this version posted August 31, 2020. The copyright holder for this preprint (which was not certified by peer review) is the author/funder. All rights reserved. No reuse allowed without permission.

condensates and RLD-RNA condensates. These results are consistent with the idea that interfacial tension of a fluid-fluid interface is determined by the intermolecular interactions of the two given fluids at a known thermodynamic state[56]. Combining the results shown in **Figure 4** with those in **Figure 1**, we propose that tuning the molecular interactions between components present on the surfaces of coexisting droplets is sufficient to control the multiphasic coexistence pattern (**Fig. 4e**). To experimentally test this idea, we designed an all K-variant of RLD (KLD: $[KGKGG]_5$, **Table S2**) that selectively weakens the PLD-RLD interactions while preserving the ability to phase separate with RNA. The R-to-K substitution is designed based on prior studies showing that (**i**) lysine residues have a much lesser potency (as compared to arginine residues) to interact with tyrosine and other π-rich amino acids/nucleobases[21,28,29,46,57,58], and (**ii**) KLDs can phase separate with RNA via ionic interactions since lysine is expected to carry a similar charge to that of arginine[28]. Indeed, our state diagram analysis indicates that KLD has no impact on PLD phase separation, even at KLD concentrations that are 20 times more than the PLD concentration (**Fig 5a**). Simultaneously, we confirmed that KLD phase separates with RNA under similar conditions as the RLD (**Fig S15**)[28]. We further verified the lack of PLD-KLD interactions by confocal microscopy experiments, which reveal that both PLD partition and PLD apparent diffusion rate within PLD condensates remain unchanged with increasing KLD concentrations in solution (**Fig 5b, Fig. S17;** compare these results with Fig. 1a-c). Consistent with these results, PLD partitioning within KLD-RNA condensates remained very low (< 1.0) and unchanged at variable RNA-to-KLD mixing ratio (**Fig. S18**), further confirming the absence/insignificance of PLD-KLD (and PLD-RNA) interactions. Therefore, the R-to-K substitution successfully abrogates PLD-RLD interactions by eliminating Arg-Tyr interactions[21].

Next, we probed for the coexistence pattern of PLD and KLD-RNA condensates. As expected, we observed that the two types of droplets (PLD homotypic and KLD-RNA heterotypic) do not share any interface (non-engulfment) at all the tested RNA-to-KLD stoichiometric ratios (**Fig 5c, Fig. S15**). These results confirm that the stability of a shared interface is critically contingent on the presence of PLD-RLD interactions at the surfaces of these two condensates. Consistent with this, we further observed that a π-rich peptide variant of the KLD, $[KGYGG]_5$, which enhances the PLD phase separation (**Fig. S19a**), restores the partial engulfment topology of ternary PLD-KLD-RNA condensates (**Fig. S19b)**. Overall, these findings suggest that sequence-encoded molecular interactions at a liquid-liquid interface between two condensed phases have a direct role in dictating the respective morphological pattern of these coexisting phases (**Fig. 5a-d**).

According to our model and experimental data (**Fig. 4**), RNA-rich RLD condensates do not share a significant interface with the PLD condensates due to the absence of PLD-RNA interactions (**Fig. 4e**). We posit that the addition of an RNA-binding module to the PLD could aid in lowering the interfacial tension between the condensates and thereby forming a shared interface with the RNA-rich RLD condensates. We tested this idea by utilizing the full-length FUS (Fused in Sarcoma), which is composed of a PLD (FUS^{PLD}) and an RNA binding domain (FUS^{RBD}) (**Fig. 5e**). The full-length FUS (FUS^{FL}) showed enhanced partition into RLD-RNA condensates (as compared to FUS^{PLD}, **Fig. 1h**) across all RNA-to-RLD mixing ratios (**Fig. S20**). Additionally, MD simulations indicate

bioRxiv preprint doi: https://doi.org/10.1101/2020.08.30.273748; this version posted August 31, 2020. The copyright holder for this preprint (which was not certified by peer review) is the author/funder. All rights reserved. No reuse allowed without permission.

that FUS^{FL} is recruited on the surface of RLD-RNA droplets at both low and high RNA concentrations (**Fig. S21**). These results confirm that FUS interacts with both RLD-rich and RNA-rich condensates. Consistent with our prediction and computational data, confocal microscopy imaging of co-existing homotypic FUS^{FL} droplets and heterotypic RLD-RNA droplets revealed that FUS^{FL} droplets completely engulf the RNA-RLD droplets (i.e. a significant interfacial contact area) across all tested RNA-to-RLD mixing ratios (**Fig. 5f and Fig. S22**). Furthermore, weakening the FUS-RLD interactions by replacing RLD with its R-to-K variant (KLD: $[KGKGG]_5$) resulted in a partially engulfed topology (**Fig. 5g and Fig. S23**). Interestingly, these FUS-KLD-RNA multiphasic condensates displayed topologies that are reminiscent of Janus spheres[59,60] with two compositionally distinct lobes (**Fig. 5g and Fig. S23**). Taken together, these results confirm that modular intermolecular interactions directly govern the coexistence pattern for multiphasic condensates by controlling the dominant interactions at the liquid-liquid interface.

Stability diagram of multiphasic condensates establishes a link between intermolecular interactions, interfacial tensions, and experimentally-observed condensate topologies

Our experimental results and computational modeling presented here collectively suggest a clear relation between the microscopic intermolecular interactions and the mesoscopic multiphase structuring that transcends length-scales. By comparing our experimental and MD simulation data with our fluid-interface modeling results (**Fig. 4**), we infer that interplay between various intermolecular interactions amongst components (PLD, RLD, and RNA) determine the relative rank order of interfacial tensions between the coexisting liquids. To verify this idea, we consider the equilibrium configurations of two immiscible droplets (PLD droplet and RLD-RNA droplet) in water as a function of the relative values of their interfacial tensions. Since all of our multiphasic condensate analysis was performed at the same conditions for PLD condensates, we chose to fix the surface tension of PLD droplets (γ_{PLD}) and vary the surface tension of RLD-RNA droplets (γ_{RLD}) and the interfacial tension between PLD droplets and RLD-RNA droplets ($\gamma_{RLD-PLD}$). Employing fluid-interface modeling, we construct a topological stability diagram (**Fig. 6a**) that marks the boundaries between three distinct morphological states (non-engulfing, partially engulfing, and complete engulfing) in terms of the relative values of these interfacial tensions (*i.e.* in terms of $\gamma_{RLD}/\gamma_{PLD}$ and $\gamma_{RLD-PLD}/\gamma_{PLD}$). This stability diagram identifies possible transition pathways between different ternary condensate topologies, which were observed in our experiments (**Fig. 6a**). We note that our stability diagram is able to capture all the variable morphologies observed in experiments, indicating that tuning interfacial tensions may be sufficient to encode diverse multiphasic patterning of the two-condensate system. Subsequently, based on our experimental data and MD simulation results (**Figs. 4&5**), we propose a mechanistic model that connects the RNA-dependent RLD and PLD interactions with the fluid-fluid interfacial interactions in the mesoscale. The transition between total engulfment to partial and non-engulfment with increasing RNA concentrations (**Fig. 4b**) can be recapitulated in simulations by varying $\gamma_{RLD-PLD}/\gamma_{PLD}$ while keeping the other interfacial tensions unchanged (**Fig. 6b;** Pathway-A). By casting this transition (Pathway-A) in **Figure 6b** onto the experimental data shown in **Figure 4b**, we can deduce that increasing RNA-to-RLD ratio increases the interfacial energy

bioRxiv preprint doi: https://doi.org/10.1101/2020.08.30.273748; this version posted August 31, 2020. The copyright holder for this preprint (which was not certified by peer review) is the author/funder. All rights reserved. No reuse allowed without permission.

between RLD-RNA droplets and PLD droplets. This is expected since RNA-PLD interactions (which dominate the interface at excess RNA conditions) are significantly weaker than RLD-PLD interactions (which dominate the interface at excess RLD conditions**, Fig. 1a-c & Fig. S4**). However, we note that Pathway-A may not be unique and a more complex pathway (such as Pathway-B) is also possible due to a simultaneous change in γ_{RLD}, and hence $\gamma_{RLD}/\gamma_{PLD}$, as a function of RNA. Replacing arginine with lysine abolishes RLD-PLD interactions, leading to an overall non-engulfment morphology (**Fig. 6a;** Pathway-B, **Fig. 5c**). Next, covalent coupling of PLD with an RNA-binding module creates a bi-valent scaffold (i.e., FUS^{FL}) with independent sites for RLD and RNA binding, which manifests in completely engulfed ternary topologies in an RNA-independent manner (**Fig. 6a**-Pathway-C; **Fig. 5e-f**). Subsequent weakening of RLD-FUS interactions via R-to-K substitutions leads to the formation of partially engulfed Janus-like topologies (**Fig 6a**-Pathway-D, **Figs. 5g** and **S23**). Taken together, these results enable us to reliably correlate sequence-encoded intermolecular interactions with multiphasic behavior, leading to coexistence patterns that can be controlled by sequence perturbations as well as mixture composition (**Fig. 6c-f**).

CONCLUSION AND OUTLOOK

Intracellular biomolecular condensates encompass a plethora of multivalent proteins and RNAs, which constitute a dense intermolecular interaction network[61]. The fluid structure of these multi-component condensates typically shows coexisting layers of liquid phases as opposed to a well-mixed isotropic liquid condensate. Here, we report experimental and computational evidence of a minimal ternary bio-condensate forming system displaying a rich variety of multiphasic structuring and spatial organization that are primarily governed by composition-dependent and sequence-encoded intermolecular interactions. *First*, we showed that varying RNA-to-RLD mixing ratio changes the mesoscale organization of the condensed phase at the single condensate level (**Fig. 1**). The distinction between the core and surface compositions of RNA-RLD condensates can be attributed to differential solvation of non-stoichiometric RLD-RNA complexes at compositionally disproportionate mixtures[49] (**Fig. 1d**). For example, in RNA-rich condensates, an unbound or partially-complexed RNA chain is expected to have a larger effective solvation volume as compared to fully complexed RLD-bound RNA chains, resulting in free RNA chains being preferentially positioned on the condensate surface[49,62] (**Fig. 1d-e**). A similar argument can also be made for RLD-rich condensates, leading to a composition-dependent tuning of the condensate surface architecture. Such organizational tuning is perceived to be a general phenomenon for heterotypic condensates and is likely to be functionally important in regulating client recruitment and controlling their spatial sub-organelle localization (**Fig. 1e-k**).

Second, we demonstrate that multiphasic condensates can form in a minimal ternary system via molecular competition for a shared binding partner. In the case of PLD-RLD-RNA system, RLD-RNA interactions dominate over PLD-RLD and this competition leads to an RNA-induced demixing of PLD and RLD into two immiscible phases from a single associative well-mixed RLD-PLD condensed phase (**Fig. 3**). The coexisting

bioRxiv preprint doi: https://doi.org/10.1101/2020.08.30.273748; this version posted August 31, 2020. The copyright holder for this preprint (which was not certified by peer review) is the author/funder. All rights reserved. No reuse allowed without permission.

droplets offer distinct microenvironments and display selective client partitioning. We envision that the sequence and structure of RNA would strongly regulate the extent of this demixing phenomenon. We also speculate that competitive inhibition of aberrant intermolecular interactions between protein and RNA components can provide an attractive route to target certain bio-condensate microenvironments in human pathologies.

Third, we show that the coexistence patterning between homotypic PLD condensates and RNA-RLD condensates is directly related to the PLD-RLD interactions at the fluid-fluid interface (**Figs. 4&5**). More specifically, our experiments and simulations suggest that PLD-RLD interactions govern the thermodynamic stability of a shared interface between PLD condensates and RLD-RNA condensates. As such, perturbation of PLD-RLD interactions on the condensate surface affects the inter-condensate interactions and hence, the interfacial tensions of the coexisting liquid phases. We report two mutually exclusive mechanisms to control the stability of a shared interface: (1) RNA dose-dependent regulation of PLD-RLD interactions through molecular competition (**Fig. 4**), and (2) perturbation of protein-protein intermolecular interaction network via RLD and PLD sequence variations, which in turn eliminates or enhances the interfacial interactions between PLD condensates and RNA-RLD condensates (**Fig. 5**). We note that our proposed **mechanism 1** is unique to heterotypic condensates where the surface composition of the condensate can be distinct from the condensate core (**Fig. 1**). We further note a distinction between the composition-dependent regulation of interfacial energies in our ternary system, which is exclusively comprised of intrinsically disordered polymers, and a recently suggested mechanism for the coexistence of stress granules (SGs) and P-bodies (PBs)[31], where a distinct protein with a common preference for both SGs and PBs acts as a “bridge” between the two condensate types and controls the shared interfacial area. In the later case[31], the relative amount of the bridge protein is an important variable in dictating the multiphase coexistence pattern. However, our results presented here for RNA-RLD condensates’ multiphasic patterning with PLD condensates reveal a unique role of the condensates’ surface organization, which can be manipulated by varying the mixture composition. This is a direct result of the formation of fuzzy non-stoichiometric protein-RNA complexes at disproportionate mixture compositions[28,49]. In such a case, an RLD-rich protein-RNA complex, *but not an RNA-rich protein-RNA complex*, can act as an *emergent molecular bridge* between RLD-RNA condensates and PLD condensates (**Fig. 4e**). This allows control over the coexistence patterns in our minimal system without additional bridging proteins.

Together, our presented experimental and computational results highlight hitherto unknown physical principles for multi-component phase separation and suggest that overlapping protein-protein and protein-RNA *fuzzy interactions* are a regulatory paradigm for the organization of multiphasic biomolecular condensates. They also provide simple physical rules to utilize the phase separation of ternary biopolymeric mixtures to create soft Janus-like particles with tunable morphologies in a stimuli-responsive fashion.

bioRxiv preprint doi: https://doi.org/10.1101/2020.08.30.273748; this version posted August 31, 2020. The copyright holder for this preprint (which was not certified by peer review) is the author/funder. All rights reserved. No reuse allowed without permission.

FIGURES AND LEGENDS

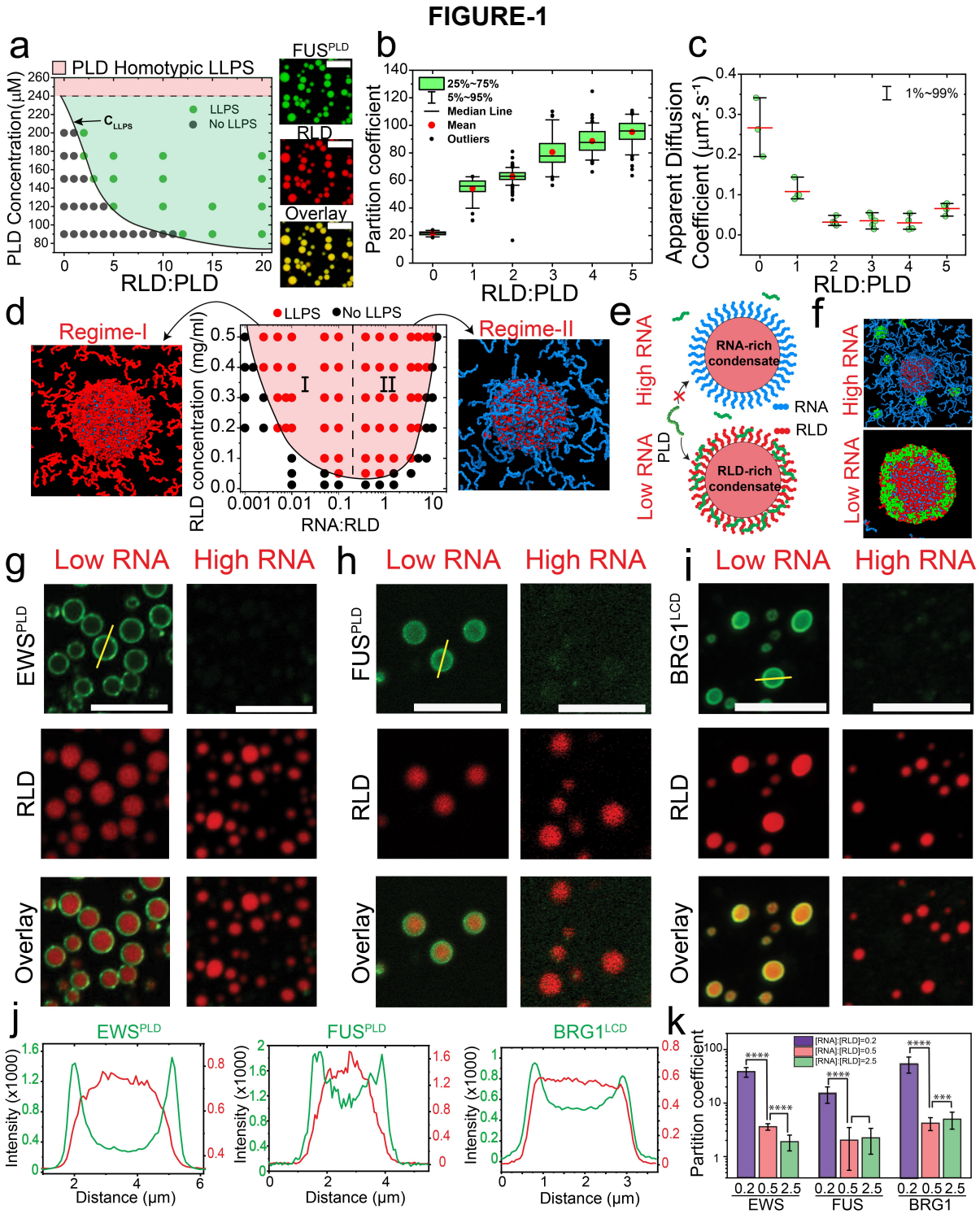

Figure 1. Mixture composition controls the structure and dynamics of binary condensates. (a) *Left:* State diagram of PLD-RLD mixtures, showing an RLD, $[RGRGG]_5$, facilitates PLD phase-separation with increasing RLD:PLD mixing ratio (mole:mole). Shaded green region shows

bioRxiv preprint doi: https://doi.org/10.1101/2020.08.30.273748; this version posted August 31, 2020. The copyright holder for this preprint (which was not certified by peer review) is the author/funder. All rights reserved. No reuse allowed without permission.

co-phase-separation regime for PLD-RLD (PLD homotypic saturation concentration: C_{sat} = 240 μM). Shaded regions are drawn as a guide to the eye. *Right*: Representative multicolor confocal fluorescence microscopy images of PLD-RLD condensates. Scale bars represent 20 μm. **(b)** PLD partition, and **(c)** PLD diffusion rate in PLD-RLD condensates at variable RLD-to-PLD mixing ratios (mole/mole). **(d)** *Center:* State diagram of RLD-RNA mixtures, showing a non-monotonic reentrant phase behavior with increasing RNA:RLD mixing ratio (wt/wt). Shaded red region shows the phase-separation regime and is drawn as a guide to the eye. Equilibrium MD configurations showing condensates with RLD-enriched surfaces at $C_{RNA} = 0.5 \times C_{RLD}$ (*left*), and condensates with RNA-enriched surfaces at $C_{RNA} = 1.7 \times C_{RLD}$ (*right*). RLD: *red*; RNA: *blue*. C_{RLD} = 1.3 mg/ml. **(e)** A schematic diagram showing that RLD decorates the RLD-RNA condensates' surface at $C_{RLD} > C_{RNA}$ while RNA surface enrichment occurs at $C_{RNA} > C_{RLD}$, which leads to differential surface recruitment of a PLD client (shown in green) in the two types of condensates. **(f)** Equilibrium MD configurations showing surface recruitment of PLD clients (*green*) in RLD-RNA droplets at low-RNA conditions ($C_{RNA} = 0.5 \times C_{RLD}$), while high-RNA conditions ($C_{RNA} = 1.7 \times C_{RLD}$) result in no PLD recruitment. RLD: *red*; RNA: *blue*. C_{RLD} = 1.3 mg/ml, C_{PLD} = 0.4 mg/ml. **(g-i)** Multicolor confocal fluorescence microscopy images showing the recruitment behavior of EWS^{PLD}, FUS^{PLD} and $BRG1^{LCD}$ into RLD-RNA droplets at variable RNA-to-RLD ratios. Scale bars represent 10 μm. **(j)** Intensity profiles across RLD-RNA condensates at low RNA concentration (*indicated by yellow lines in **g,h&i***) with EWS^{PLD} (*left*), FUS^{PLD} (*center*), $BRG1^{LCD}$ (*right*) showing preferential client recruitment (green) on the condensate surface. **(k)** Client partition coefficient in RLD-RNA condensates at variable RNA-to-RLD mixing ratios for FUS^{PLD}, EWS^{PLD}, and $BRG1^{LCD}$ (*See SI for box plots*). Error bars represent ± 1 s.d. For **g-k**, samples were prepared at [FUS^{RGG3}]=1 mg/ml and at a poly(U) to FUS^{RGG3} ratio of 0.2 (wt/wt) for low RNA and 2.5 (wt/wt) for the high RNA case or as indicated. For **d&f,** RLD=FUS^{RGG3}; RNA=poly(U). For **a-c&f,** PLD=FUS^{PLD}. All samples were prepared in a 25 mM Tris-HCl (pH 7.5) buffer containing 150 mM NaCl and 20 mM DTT.

bioRxiv preprint doi: https://doi.org/10.1101/2020.08.30.273748; this version posted August 31, 2020. The copyright holder for this preprint (which was not certified by peer review) is the author/funder. All rights reserved. No reuse allowed without permission.

FIGURE-2

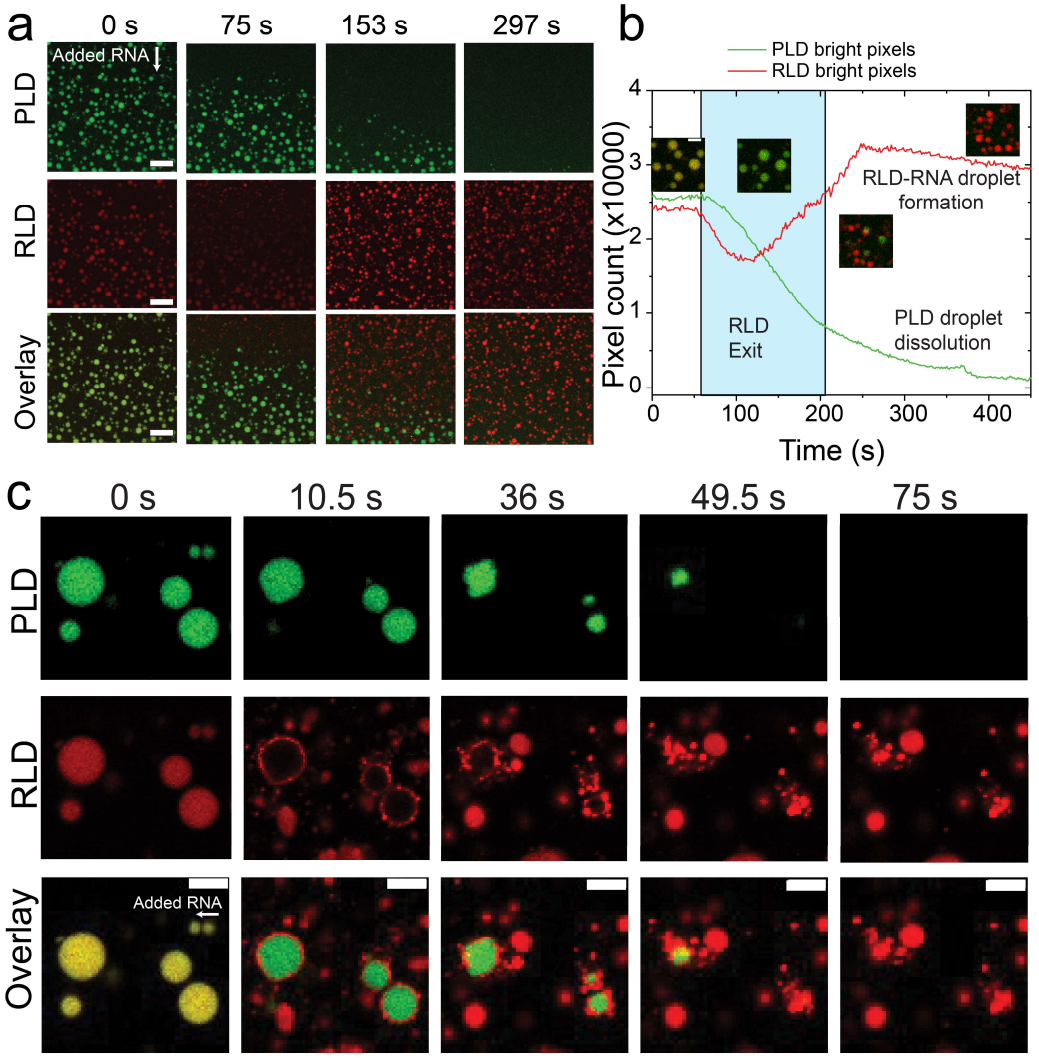

Figure 2. RNA induces a condensate switching from PLD-RLD to RLD-RNA. (a) Multicolor confocal fluorescence time-lapse images showing dissolution of PLD-RLD (RLD: FUS^{RGG3}) droplets and subsequent formation of RLD-RNA droplets upon addition of poly(U) RNA. Scale bar = 20 µm. **(b)** Plot of the total area covered by condensates in the green (PLD) and red (RLD) channels for the data shown in (**a**) and in **Movie S1**. The areas were calculated by counting the green pixels (for PLD) and the red pixels (for RLD) and plotted as a function of time. The images indicate the various stages of sample evolution after RNA addition. The *white* region (*left*) indicates the time-window where PLD and RLD co-localize; the *cyan* shaded region indicates the time-window when RLD is leaving the PLD-RLD condensates; the *white* region (*right*) indicates the subsequent dissolution of PLD-RLD condensates and the formation of RLD-RNA condensates. Scale bar represents 5 µm. **(c)** Same assay as (**a**) but with poly(A) RNA. (RLD: $[RGRGG]_5$). Scale bars represent 4 µm. All samples were prepared in 25 mM Tris-HCl, 150 mM NaCl and 20 mM DTT buffer. PLD: FUS^{PLD}.

bioRxiv preprint doi: https://doi.org/10.1101/2020.08.30.273748; this version posted August 31, 2020. The copyright holder for this preprint (which was not certified by peer review) is the author/funder. All rights reserved. No reuse allowed without permission.

FIGURE-3

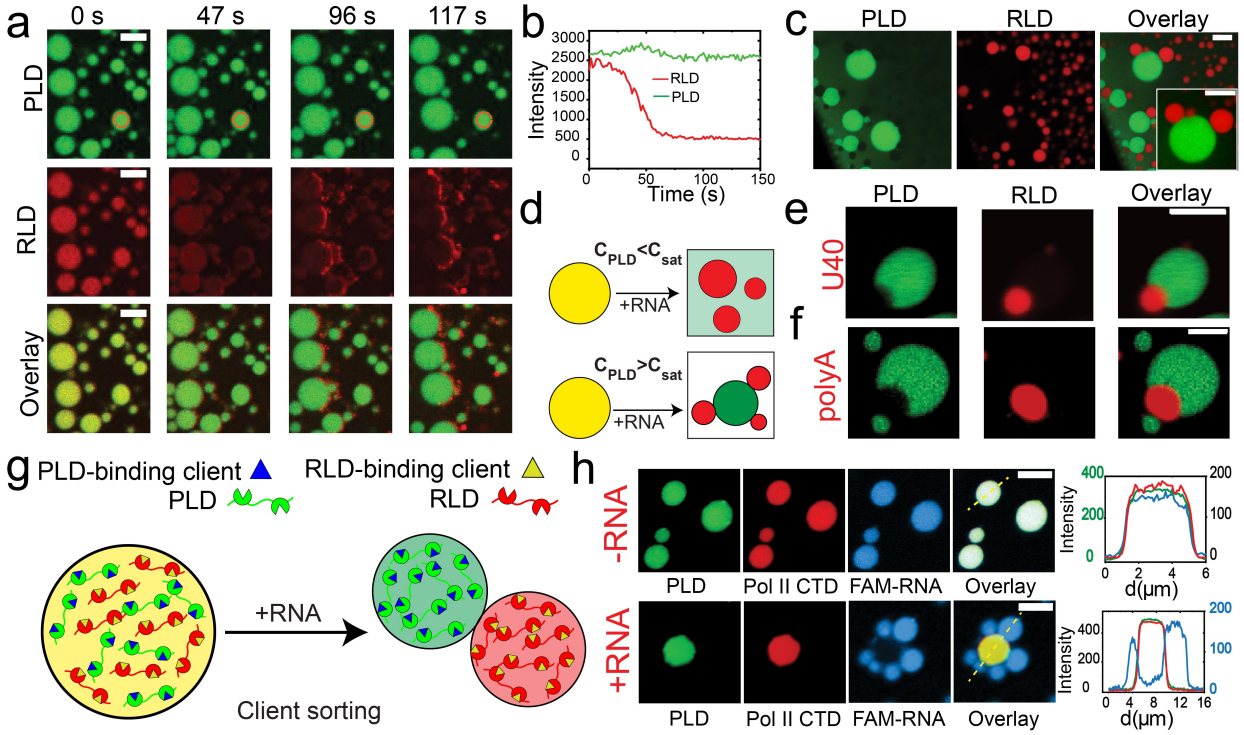

Figure 3. RNA causes demixing of RLD and PLD. (a) Multicolor confocal fluorescence time-lapse images showing the sequestration of RLD (FUS^{RGG3}) from PLD-RLD droplets and the subsequent formation of RLD–RNA droplets upon addition of poly(U) RNA. [PLD]=250 μM; [FUS^{RGG3}]=750 μM or 2.6 mg/ml; and poly(U) RNA is added to a final concentration of 13.0 mg/ml. **(b)** PLD and RLD intensities as a function of time within a PLD-RLD condensate [*red circle* in (**a**)]. **(c)** Co-existing PLD homotypic droplets and RLD-RNA heterotypic droplets. Images were collected 20 minutes after RNA addition. [PLD]=250 μM; [FUS^{RGG3}]=1250 μM (4.3 mg/ml); and poly(U) RNA is added to a final concentration of 10.8 mg/ml. **(d)** A schematic diagram summarizing the effect of RNA on PLD-RLD condensates. **(e)** Fluorescence microscopy images of the coexisting PLD condensates (green) and RLD-RNA condensates (red) prepared using U40 RNA. Each type of droplets was prepared independently at initial concentrations of [PLD]=400 μM, [FUS^{RGG3}]=4.0 mg/ml and [U40]=4.0 mg/ml and then mixed (1:1 by volume). **(f)** Fluorescence images of the coexisting PLD condensates (green) and RLD-RNA condensates (red) prepared using poly(A) RNA. **(g)** A schematic showing that RNA-induced de-mixing of PLD-RLD condensate (yellow) into PLD (green) and RLD-RNA (red) condensates can sort diverse clients into different condensates. **(h)** Fluorescence micrographs and intensity profiles showing recruitment of two clients, FAM-labeled RNA client and Alexa488-labeled Pol II CTD, into the PLD-RLD condensates in the absence of RNA (*top*) and the differential recruitment of the same clients–FAM-RNA (blue) into heterotypic RLD-RNA condensates and Pol II CTD (red) into homotypic PLD condensates–in the presence of poly(U) RNA (*bottom*). PLD condensates prepared at 400 μM were mixed (1:1 by volume) with a sample containing 4.0 mg/ml $[RGRGG]_5$ and 0.0 mg/ml (*top*) or 8.0 mg/ml (*bottom*) of poly(U) RNA. All samples were prepared in 25 mM Tris-HCl, 150 mM NaCl and 20 mM DTT buffer. PLD = FUS^{PLD}. Scale bar = 10 μm for (**a&c**) and 5 μm for (**e-h**).

bioRxiv preprint doi: https://doi.org/10.1101/2020.08.30.273748; this version posted August 31, 2020. The copyright holder for this preprint (which was not certified by peer review) is the author/funder. All rights reserved. No reuse allowed without permission.

FIGURE-4

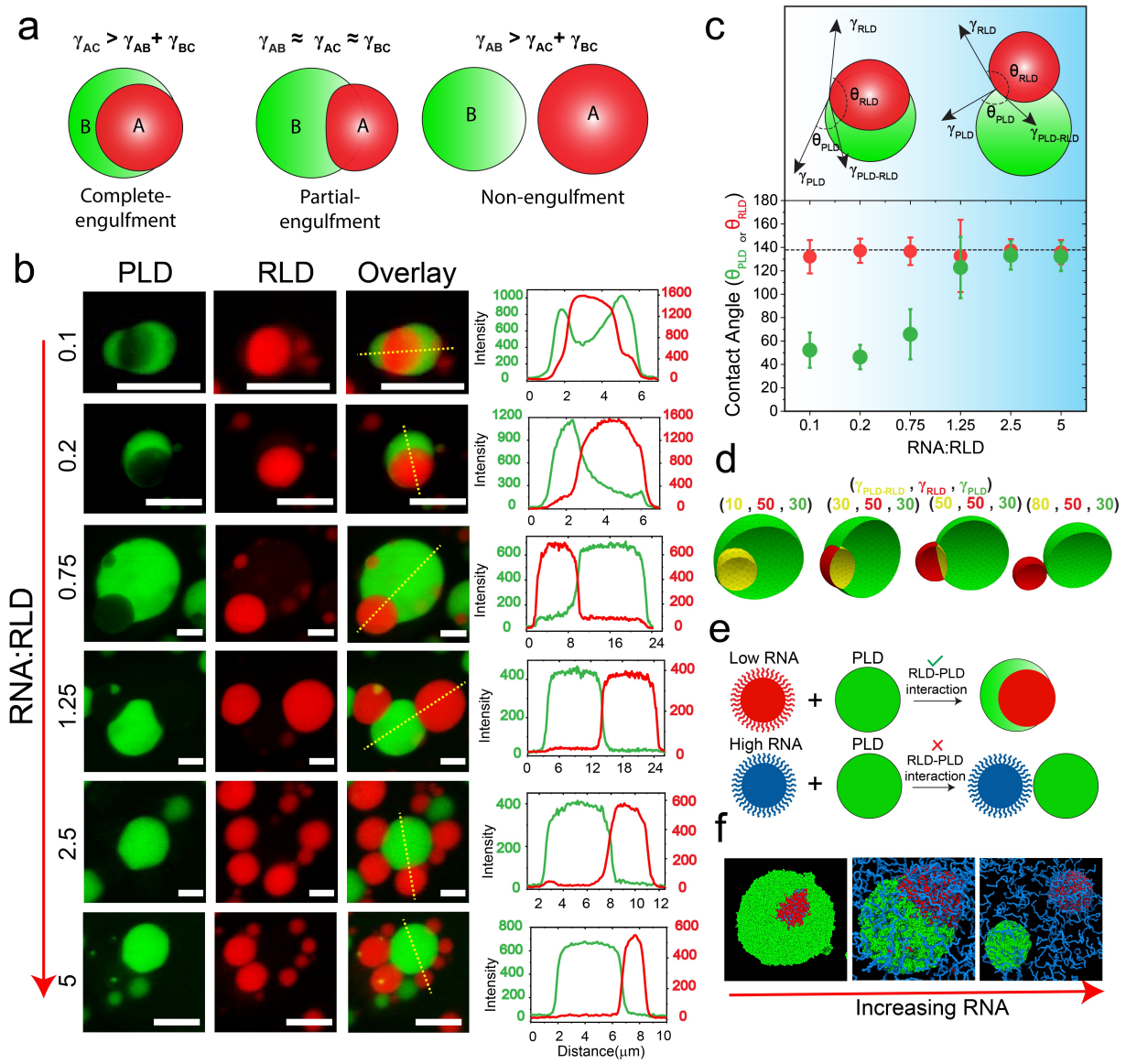

Figure 4. RNA-to-RLD ratio tunes the morphology of co-existing condensates. (a) A schematic diagram showing that relative ranking of interfacial tensions dictates the morphology of the biphasic condensates (A-droplet, B-droplet, C-dispersed phase). **(b)** Fluorescence microscopy images and intensity profiles for co-existing homotypic PLD droplets (green) and heterotypic RLD-RNA condensates (red) at different RNA-to-RLD ratios. Each type of droplets was separately prepared at initial concentrations of [PLD]=400 μM, $[RGRGG]_5$=4.0 mg/ml and variable poly(U) RNA-to-RLD ratios (wt/wt), as indicated and then mixed (1:1 vol/vol). All samples were prepared in 25 mM Tris-HCl, 150 mM NaCl and 20 mM DTT buffer. All Scale bars represent 10 μm. **(c)** Contact angle plot (*bottom*) for co-existing PLD (θ_{PLD} in green) and RLD-RNA (θ_{RLD} in red) condensates for all the samples shown in (**b**). Dashed line represents the average value of θ_{RLD} across all samples. Error bars represent ± 1 s.d. (*Top*) A schematic showing the co-existing condensate morphology at low and high θ_{PLD}. Color gradient (blue) represents the

bioRxiv preprint doi: https://doi.org/10.1101/2020.08.30.273748; this version posted August 31, 2020. The copyright holder for this preprint (which was not certified by peer review) is the author/funder. All rights reserved. No reuse allowed without permission.

increasing RNA concentration. **(d)** Coexistence patterns of a model doublet-of-droplet as a function of interfacial tensions calculated using a fluid interfacial modeling tool (Surface Evolver[55]). **(e)** Proposed mechanism of RNA-mediated fluid-fluid interface regulation. At low RNA concentration, RNA-RLD condensates (red) are enriched with RLD chains on their surfaces, thus facilitating RLD-PLD interfacial binding and mediating a wetting behavior. At high RNA concentration, RLD-RNA condensate surfaces (blue) are enriched with RNA chains, limiting the available RLD molecules for PLD binding, which is responsible for minimal wetting behavior with PLD condensates (green). **(f)** Equilibrium MD snapshots at variable RNA-to-RLD mixing ratios (see **Fig. S16b** for the corresponding density profiles). (RLD=FUS^{RGG3}, red; RNA= poly(U), blue; PLD=FUS^{PLD}, green). C_{RLD}=5.6 mg/ml, RNA-to-RLD ratio=0.3, 1.8, 3.2 (respectively for the three snapshots shown), C_{PLD}=7.22 mg/ml.

bioRxiv preprint doi: https://doi.org/10.1101/2020.08.30.273748; this version posted August 31, 2020. The copyright holder for this preprint (which was not certified by peer review) is the author/funder. All rights reserved. No reuse allowed without permission.

FIGURE-5

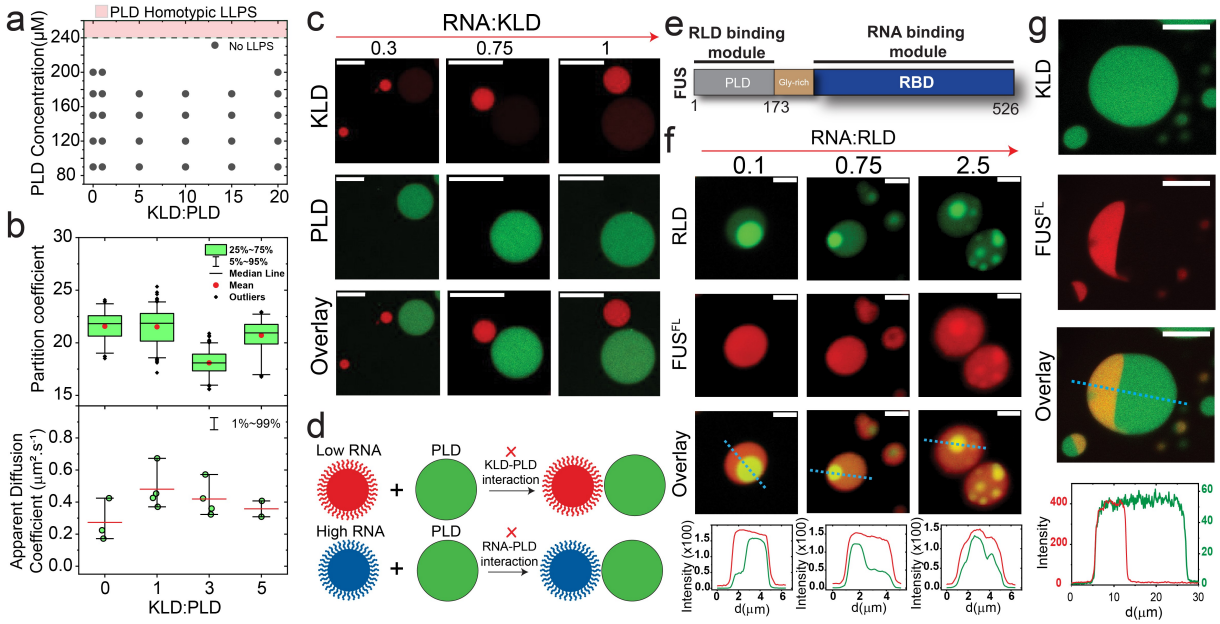

Figure 5. Intermolecular interactions between RNA and protein components tune the morphology of co-existing condensates (a) State diagram of PLD-KLD mixtures as a function of KLD-to-PLD ratio (mole:mole), showing that a KLD, $[KGKGG]_5$, *has no effect* on PLD phase-separation (compare with **Fig. 1a** for RLD-PLD mixtures). **(b)** PLD partition coefficient and diffusion rate in PLD-KLD condensates as a function of KLD to PLD mixing ratio (mole:mole). **(c)** Fluorescence images showing that the morphology of coexisting PLD homotypic condensates and KLD-RNA condensates is non-engulfing and does not vary with RNA-to KLD stoichiometry. Each type of droplets was separately prepared at initial concentrations of $[FUS^{PLD}]$=400 μM, $[KGKGG]_5$=4 mg/ml and variable poly(U) RNA-to-KLD ratios (wt/wt), as indicated, and mixed (1:1 vol/vol). **(d)** Schematic showing that due to insignificant KLD-PLD interfacial interactions, the PLD homotypic and KLD-RNA heterotypic condensates do not share any interface (non-engulfment) at both low and high RNA. **(e)** Domain architecture of FUS^{FL} showing both PLD and RBD modules. **(f)** Fluorescence microscopy images and intensity profiles for co-existing homotypic FUS^{FL} droplets (red) and heterotypic RLD-RNA condensates at different RNA-to-RLD ratio. Each type of droplets was separately prepared at initial concentrations of $[FUS^{FL}]$=21.3 μM, $[FUS^{RGG3}]$=1 mg/ml and variable poly(U) RNA-to-RLD ratios (wt/wt), as indicated, and mixed (1:1 vol/vol). **(g)** Fluorescence micrographs and intensity profiles for Janus droplets formed by coexisting homotypic FUS^{FL} droplets (red) and heterotypic KLD-RNA condensates (green). Each type of droplets was separately prepared at initial concentrations of $[FUS^{FL}]$=22 μM, $[KGKGG_5]$=4 mg/ml and poly(U)=3 mg/ml and mixed (1:1 vol/vol). All samples were made in a buffer containing 25 mM Tris-HCl, 150 mM NaCl and 20 mM DTT. Scale bars represent 10 μm for (**c&g**) and 2 μm for (**f**).

bioRxiv preprint doi: https://doi.org/10.1101/2020.08.30.273748; this version posted August 31, 2020. The copyright holder for this preprint (which was not certified by peer review) is the author/funder. All rights reserved. No reuse allowed without permission.

FIGURE-6

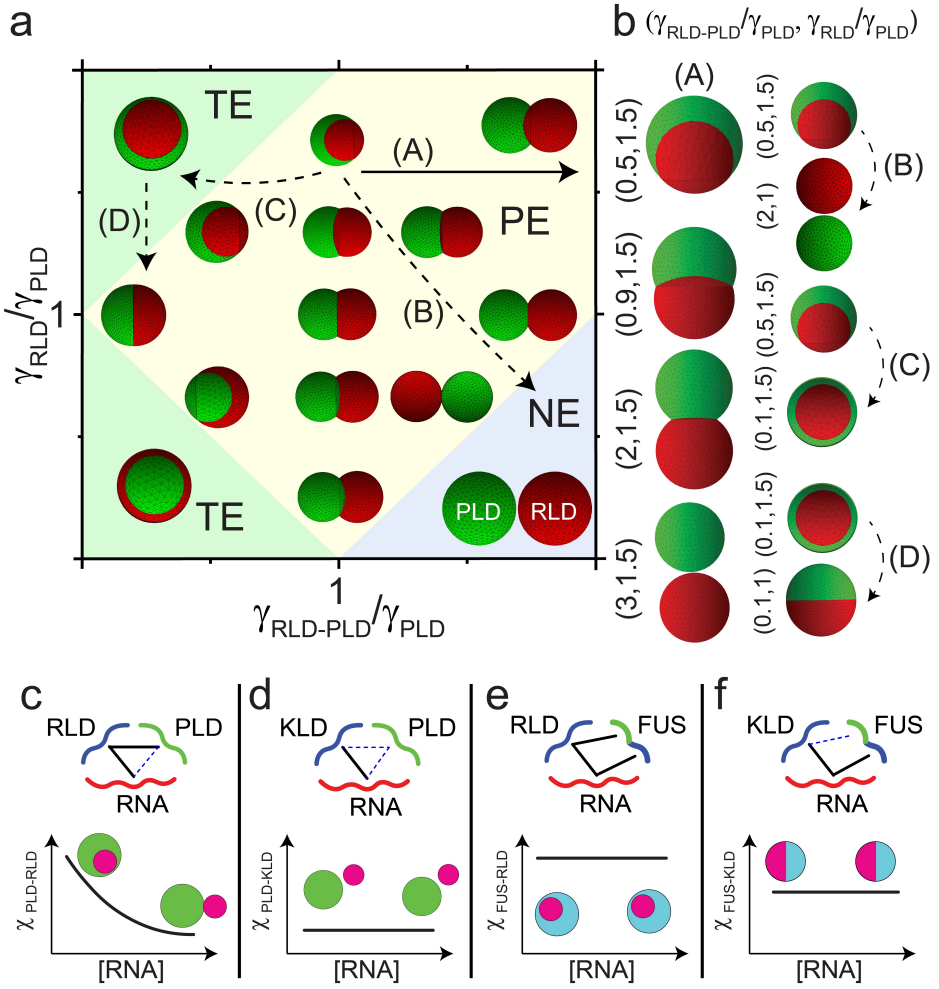

Figure 6. Stability diagram of a pair of coexisting condensates provides a link between intermolecular interactions and multiphasic topology. (a) Topological stability diagram for PLD droplets coexistence pattern with RLD-RNA droplets from fluid-interface modeling simulations. In these simulations, γ_{PLD} was fixed and γ_{RLD} and $\gamma_{RLD-PLD}$ were varied. The shaded regions mark the different topological states: total engulfment (TE), partial engulfement (PE), and non-engulfment (NE). The solid arrows indicate a *continuous* morphological transitions with RNA dosage as described in the text. The dashed lines correspond to *discrete* transitions due to sequence variations. **(b)** Simulation strips showing the continuous and discrete morphological transitions as the values of the interfacial tensions are varied along the corresponding arrows in the stability diagram in **(a)**. **(c-f)** Schematic diagrams showing the interactions between the ternary components as well as the observed morphology as a function of RNA concentration. The schematic plots show how the interactions between the two types of droplets (χ) are expected to change as a function of RNA dosage. The solid lines in the schematic interaction diagrams indicates strong interactions while the dashed line indicate weak and/or absent interactions.

bioRxiv preprint doi: https://doi.org/10.1101/2020.08.30.273748; this version posted August 31, 2020. The copyright holder for this preprint (which was not certified by peer review) is the author/funder. All rights reserved. No reuse allowed without permission.

MATERIALS AND METHODS

Details and protocols for the expression/purification of proteins, protein/RNA sample preparation, state diagram measurements, turbidity measurements, confocal imaging and partition analyses, FRAP, RNA-induced condensate switching and demixing, FCS, contact angle analysis, molecular dynamics simulation, fluid-interface simulations and other relevant experimental procedures are provided in the supplementary information appendix.

ACKNOWLEDGEMENTS

The authors gratefully acknowledge UB north campus confocal imaging facility and its director, Mr. Alan Siegel for helpful assistance. The authors acknowledge Ms. Liz-Audrey Djomnang Kounatse for her help with FUS^{RGG3}-poly(U) phase diagram. The authors also acknowledge helpful discussions with Dr. George Thurston, and Dr. Mahdi M. Moosa at various stages of manuscript preparation. We gratefully acknowledge support for this work from University at Buffalo, SUNY, College of Arts and Sciences to P.R.B. and funding from the National Institute of General Medical Sciences (NIGMS) of the National Institutes of Health (R35 GM138186) to P.R.B. D.A.P. acknowledges financial support from Iowa State University. D.A.P. also acknowledges NSF Extreme Science and Engineering Discovery Environment allocation on Bridges graphical processing unit machine at the service provider through Allocation CTS190023.

AUTHOR CONTRIBUTIONS

P.R.B. and T.K. conceived the idea and designed the experiments. T.K. performed the experiments and analyzed the data with help from P.R.B. and I.A. R.B.D. expressed and purified recombinant proteins and performed their fluorescent labeling. I.A. performed the fluid-interface modeling simulations. M.R. and D.A.P. designed and performed the MD simulations. P.R.B., T.K., and I.A. wrote the manuscript with input from R.B.D., M.R., and D.A.P.

DATA AVAILABILITY

All data supporting the findings of this study is included in this paper and in the supplementary information. Additional data are available from the corresponding author upon reasonable request.

CODE AVAILABILITY

We used the publicaly available HOOMD-blue package (v2.7.0)[63] for molecular dynamics simulations. Fluid-interface modeling was done using the freely available software SurfaceEvolver (v2.70)[55]. Custom codes for the analysis and production of the results reported in this paper can be made available from the corresponding author upon reasonable request.

CONFLICT OF INTEREST

bioRxiv preprint doi: https://doi.org/10.1101/2020.08.30.273748; this version posted August 31, 2020. The copyright holder for this preprint (which was not certified by peer review) is the author/funder. All rights reserved. No reuse allowed without permission.

The authors declare no conflict of interest.

bioRxiv preprint doi: https://doi.org/10.1101/2020.08.30.273748; this version posted August 31, 2020. The copyright holder for this preprint (which was not certified by peer review) is the author/funder. All rights reserved. No reuse allowed without permission.

REFERENCES

1 Banani, S. F., Lee, H. O., Hyman, A. A. & Rosen, M. K. Biomolecular condensates: organizers of cellular biochemistry. *Nature reviews Molecular cell biology* **18**, 285-298 (2017).

2 Shin, Y. & Brangwynne, C. P. Liquid phase condensation in cell physiology and disease. *Science* **357**, doi:10.1126/science.aaf4382 (2017).

3 Alberti, S. Phase separation in biology. *Current Biology* **27**, R1097-R1102, doi:https://doi.org/10.1016/j.cub.2017.08.069 (2017).

4 Forman-Kay, J. D., Kriwacki, R. W. & Seydoux, G. Phase separation in biology and disease. *Journal of molecular biology* **430**, 4603 (2018).

5 Hyman, A. A., Weber, C. A. & Jülicher, F. Liquid-liquid phase separation in biology. *Annual review of cell and developmental biology* **30**, 39-58 (2014).

6 Mitrea, D. M. & Kriwacki, R. W. Phase separation in biology; functional organization of a higher order. *Cell Communication and Signaling* **14**, 1 (2016).

7 Aguzzi, A. & Altmeyer, M. Phase separation: linking cellular compartmentalization to disease. *Trends in cell biology* **26**, 547-558 (2016).

8 Alberti, S. & Hyman, A. A. Are aberrant phase transitions a driver of cellular aging? *BioEssays* **38**, 959-968 (2016).

9 Basu, S. *et al.* Unblending of Transcriptional Condensates in Human Repeat Expansion Disease. *Cell* (2020).

10 Brangwynne, C. P., Mitchison, T. J. & Hyman, A. A. Active liquid-like behavior of nucleoli determines their size and shape in Xenopus laevis oocytes. *Proc Natl Acad Sci U S A* **108**, 4334-4339, doi:10.1073/pnas.1017150108 (2011).

11 Feric, M. *et al.* Coexisting liquid phases underlie nucleolar subcompartments. *Cell* **165**, 1686-1697 (2016).

12 Fei, J. *et al.* Quantitative analysis of multilayer organization of proteins and RNA in nuclear speckles at super resolution. *J Cell Sci* **130**, 4180-4192 (2017).

13 West, J. A. *et al.* Structural, super-resolution microscopy analysis of paraspeckle nuclear body organization. *Journal of cell biology* **214**, 817-830 (2016).

14 Jain, S. *et al.* ATPase-Modulated Stress Granules Contain a Diverse Proteome and Substructure. *Cell* **164**, 487-498, doi:10.1016/j.cell.2015.12.038 (2016).

15 Mountain, G. A. & Keating, C. D. Formation of Multiphase Complex Coacervates and Partitioning of Biomolecules within them. *Biomacromolecules* (2019).

16 Lu, T. & Spruijt, E. Multiphase complex coacervate droplets. *Journal of the American Chemical Society* **142**, 2905-2914 (2020).

17 Brangwynne, C. P., Tompa, P. & Pappu, R. V. Polymer physics of intracellular phase transitions. *Nature Physics* **11**, 899-904 (2015).

18 Choi, J.-M., Holehouse, A. S. & Pappu, R. V. Physical principles underlying the complex biology of intracellular phase transitions. *Annual Review of Biophysics* **49**, 107-133 (2020).

19 Molliex, A. *et al.* Phase separation by low complexity domains promotes stress granule assembly and drives pathological fibrillization. *Cell* **163**, 123-133, doi:10.1016/j.cell.2015.09.015 (2015).

20 Martin, E. W. & Mittag, T. Relationship of sequence and phase separation in protein low-complexity regions. *Biochemistry* **57**, 2478-2487 (2018).

bioRxiv preprint doi: https://doi.org/10.1101/2020.08.30.273748; this version posted August 31, 2020. The copyright holder for this preprint (which was not certified by peer review) is the author/funder. All rights reserved. No reuse allowed without permission.

21 Vernon, R. M. *et al.* Pi-Pi contacts are an overlooked protein feature relevant to phase separation. *Elife* **7**, e31486 (2018).

22 Chong, P. A., Vernon, R. M. & Forman-Kay, J. D. RGG/RG motif regions in RNA binding and phase separation. *Journal of molecular biology* **430**, 4650-4665 (2018).

23 Franzmann, T. & Alberti, S. Prion-like low-complexity sequences: Key regulators of protein solubility and phase behavior. *J Biol Chem*, doi:10.1074/jbc.TM118.001190 (2018).

24 Pak, C. W. *et al.* Sequence determinants of intracellular phase separation by complex coacervation of a disordered protein. *Molecular cell* **63**, 72-85 (2016).

25 Quiroz, F. G. & Chilkoti, A. Sequence heuristics to encode phase behaviour in intrinsically disordered protein polymers. *Nature materials* **14**, 1164-1171 (2015).

26 Wang, J. *et al.* A molecular grammar governing the driving forces for phase separation of prion-like RNA binding proteins. *Cell* **174**, 688-699. e616 (2018).

27 Martin, E. W. *et al.* Valence and patterning of aromatic residues determine the phase behavior of prion-like domains. *Science* **367**, 694-699 (2020).

28 Alshareedah, I. *et al.* Interplay between Short-Range Attraction and Long-Range Repulsion Controls Reentrant Liquid Condensation of Ribonucleoprotein–RNA Complexes. *Journal of the American Chemical Society* **141**, 14593-14602, doi:10.1021/jacs.9b03689 (2019).

29 Boeynaems, S. *et al.* Spontaneous driving forces give rise to protein− RNA condensates with coexisting phases and complex material properties. *Proceedings of the National Academy of Sciences* **116**, 7889-7898 (2019).

30 Mitrea, D. M. *et al.* Self-interaction of NPM1 modulates multiple mechanisms of liquid–liquid phase separation. *Nature communications* **9**, 1-13 (2018).

31 Sanders, D. W. *et al.* Competing protein-RNA interaction networks control multiphase intracellular organization. *Cell* **181**, 306-324. e328 (2020).

32 Ghosh, A., Zhang, X. & Zhou, H.-X. Tug of War between Condensate Phases in a Minimal Macromolecular System. *Journal of the American Chemical Society* **142**, 8848-8861 (2020).

33 Thandapani, P., O'Connor, T. R., Bailey, T. L. & Richard, S. Defining the RGG/RG motif. *Molecular cell* **50**, 613-623 (2013).

34 Youn, J.-Y. *et al.* Properties of Stress Granule and P-Body Proteomes. *Molecular Cell* **76**, 286-294 (2019).

35 Lopez-Gonzalez, R. *et al.* Poly (GR) in C9ORF72-related ALS/FTD compromises mitochondrial function and increases oxidative stress and DNA damage in iPSC-derived motor neurons. *Neuron* **92**, 383-391 (2016).

36 Yang, D. *et al.* FTD/ALS-associated poly (GR) protein impairs the Notch pathway and is recruited by poly (GA) into cytoplasmic inclusions. *Acta neuropathologica* **130**, 525-535 (2015).

37 Sakae, N. *et al.* Poly-GR dipeptide repeat polymers correlate with neurodegeneration and Clinicopathological subtypes in C9ORF72-related brain disease. *Acta neuropathologica communications* **6**, 63 (2018).

38 Zhang, Y.-J. *et al.* Poly (GR) impairs protein translation and stress granule dynamics in C9orf72-associated frontotemporal dementia and amyotrophic lateral sclerosis. *Nature medicine* **24**, 1136-1142 (2018).

bioRxiv preprint doi: https://doi.org/10.1101/2020.08.30.273748; this version posted August 31, 2020. The copyright holder for this preprint (which was not certified by peer review) is the author/funder. All rights reserved. No reuse allowed without permission.

39 Zhang, Y.-J. *et al.* Heterochromatin anomalies and double-stranded RNA accumulation underlie C9orf72 poly (PR) toxicity. *Science* **363**, eaav2606 (2019).

40 White, M. R. *et al.* C9orf72 Poly (PR) dipeptide repeats disturb biomolecular phase separation and disrupt nucleolar function. *Molecular cell* **74**, 713-728. e716 (2019).

41 Hartmann, H. *et al.* Proteomics and C9orf72 neuropathology identify ribosomes as poly-GR/PR interactors driving toxicity. *Life science alliance* **1** (2018).

42 Boeynaems, S. *et al.* Phase separation of C9orf72 dipeptide repeats perturbs stress granule dynamics. *Molecular cell* **65**, 1044-1055. e1045 (2017).

43 Lee, K. H. *et al.* C9orf72 Dipeptide Repeats Impair the Assembly, Dynamics, and Function of Membrane-Less Organelles. *Cell* **167**, 774-788 e717, doi:10.1016/j.cell.2016.10.002 (2016).

44 Nedelsky, N. B. & Taylor, J. P. Bridging biophysics and neurology: aberrant phase transitions in neurodegenerative disease. *Nat Rev Neurol* **15**, 272-286, doi:10.1038/s41582-019-0157-5 (2019).

45 Ross, E. D. & Toombs, J. A. The effects of amino acid composition on yeast prion formation and prion domain interactions. *Prion* **4**, 60-65 (2010).

46 Wang, J. *et al.* A Molecular Grammar Governing the Driving Forces for Phase Separation of Prion-like RNA Binding Proteins. *Cell* **174**, 688-699 e616, doi:10.1016/j.cell.2018.06.006 (2018).

47 Banerjee, P. R., Milin, A. N., Moosa, M. M., Onuchic, P. L. & Deniz, A. A. Reentrant phase transition drives dynamic substructure formation in ribonucleoprotein droplets. *Angewandte Chemie International Edition* **56**, 11354-11359 (2017).

48 Aumiller, W. M., Jr. & Keating, C. D. Phosphorylation-mediated RNA/peptide complex coacervation as a model for intracellular liquid organelles. *Nat Chem* **8**, 129-137, doi:10.1038/nchem.2414 (2016).

49 Alshareedah, I., Moosa, M. M., Raju, M., Potoyan, D. A. & Banerjee, P. R. Phase transition of RNA−protein complexes into ordered hollow condensates. *Proceedings of the National Academy of Sciences*, 201922365, doi:10.1073/pnas.1922365117 (2020).

50 Guzowski, J., Korczyk, P. M., Jakiela, S. & Garstecki, P. The structure and stability of multiple micro-droplets. *Soft Matter* **8**, 7269-7278 (2012).

51 Torza, S. & Mason, S. Coalescence of two immiscible liquid drops. *Science* **163**, 813-814 (1969).

52 Berthier, J. & Brakke, K. A. *The physics of microdroplets*. (John Wiley & Sons, 2012).

53 Correll, C. C., Bartek, J. & Dundr, M. The Nucleolus: A Multiphase Condensate Balancing Ribosome Synthesis and Translational Capacity in Health, Aging and Ribosomopathies. *Cells* **8**, 869 (2019).

54 Rowlinson, J. S. & Widom, B. *Molecular theory of capillarity*. (Clarendon Press, 1982).

55 Brakke, K. A. The surface evolver. *Experimental mathematics* **1**, 141-165 (1992).

56 Lykema, J. *et al. Fundamentals of Interface and Colloid Science, Liquid–Fluid Interfaces, vol. 3*. (Academic Press, 2000).

57 Nott, T. J. *et al.* Phase Transition of a Disordered Nuage Protein Generates Environmentally Responsive Membraneless Organelles. *Molecular Cell* **57**, 936-947, doi:10.1016/j.molcel.2015.01.013 (2015).

bioRxiv preprint doi: https://doi.org/10.1101/2020.08.30.273748; this version posted August 31, 2020. The copyright holder for this preprint (which was not certified by peer review) is the author/funder. All rights reserved. No reuse allowed without permission.

58 Brady, J. P. *et al.* Structural and hydrodynamic properties of an intrinsically disordered region of a germ cell-specific protein on phase separation. *Proc Natl Acad Sci U S A* **114**, E8194-E8203, doi:10.1073/pnas.1706197114 (2017).

59 Walther, A. & Müller, A. H. Janus particles. *Soft Matter* **4**, 663-668 (2008).

60 Casagrande, C., Fabre, P., Raphael, E. & Veyssié, M. “Janus beads”: realization and behaviour at water/oil interfaces. *EPL (Europhysics Letters)* **9**, 251 (1989).

61 Boeynaems, S. *et al.* Protein phase separation: a new phase in cell biology. *Trends in cell biology* **28**, 420-435 (2018).

62 Harmon, T. S., Holehouse, A. S. & Pappu, R. V. Differential solvation of intrinsically disordered linkers drives the formation of spatially organized droplets in ternary systems of linear multivalent proteins. *New Journal of Physics* **20**, 045002 (2018).

63 Anderson, J. A., Lorenz, C. D. & Travesset, A. General purpose molecular dynamics simulations fully implemented on graphics processing units. *Journal of computational physics* **227**, 5342-5359 (2008).